JACS
JOURNAL OF THE AMERICAN CHEMICAL SOCIETY

Article

pubs.acs.org/JACS

Crystallization Kinetics of Organic–Inorganic Trihalide Perovskites and the Role of the Lead Anion in Crystal Growth

David T. Moore,[†] Hiroaki Sai,[†,⊥] Kwan W. Tan,[†] Detlef-M. Smilgies,[‡] Wei Zhang,[§] Henry J. Snaith,[§] Ulrich Wiesner,*[,†] and Lara A. Estroff*[,†,∥]

[†]Department of Materials Science and Engineering, Cornell University, Ithaca, New York 14853, United States

[‡]Cornell High Energy Synchrotron Source (CHESS), Ithaca, New York 14853, United States

[§]Clarendon Laboratory, University of Oxford, Parks Road, Oxford OX1 3PU, United Kingdom

[∥]Kavli Institute at Cornell for Nanoscale Science, Cornell University, Ithaca, New York, 14853, United States

Supporting Information

ABSTRACT: Methylammonium lead halide perovskite solar cells continue to excite the research community due to their rapidly increasing performance which, in large part, is due to improvements in film morphology. The next step in this progression is control of the crystal morphology which requires a better fundamental understanding of the crystal growth. In this study we use in situ X-ray scattering data to study isothermal transformations of perovskite films derived from chloride, iodide, nitrate, and acetate lead salts. Using established models we determine the activation energy for crystallization and find that it changes as a function of the lead salt. Further analysis enabled determination of the precursor composition and showed that the primary step in perovskite formation is removal of excess organic salt from the precursor. This understanding suggests that careful choice of the lead salt will aid in controlling crystal growth, leading to superior films and better performing solar cells.

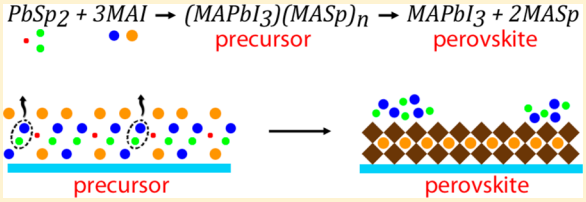

INTRODUCTION

The rapid increase in device performance reported for organic–inorganic trihalide perovskites, e.g., $(CH_3NH_3)PbI_3$, has energized the photovoltaic community's efforts to create low cost solar cells from inexpensive and abundant constituents.[1−3] Over the past year many researchers have been moving from a mesoscopic cell architecture to planar devices, with planar cells exhibiting efficiencies comparable to those of mesoscopic cells with an uncertified report of 19.3% efficiency.[4] The use of a planar architecture is predicated on the ability to fabricate continuous, conformal layers. The ability to make high efficiency planar devices is dependent on a variety of factors; however, there have been several reports that correlate both the film and crystal morphology (e.g., grain size and/or orientation) to device performance.[5−7] Thus, the control of the final film and crystal morphology is a critical parameter in achieving consistent, high performance devices, and this control will rely upon a fundamental understanding of the crystal growth, both its mechanism and kinetics. Our goal in this work is to elucidate the crystallization process of the organic–inorganic halide perovskites by an in situ X-ray scattering study of the crystal growth dynamics.

The initial application of these perovskites was as a dye replacement in dye-sensitized solar cells (DSSC) and utilized mesoporous TiO_2 as a transport material; in the past two years, device efficiencies based on this architecture have increased from ∼10% to over 17%.[8−10] However, for the most efficient devices based on mesoporous TiO_2, the thickness of the mesoporous layer has diminished to only a few hundred nanometers, and a solid polycrystalline perovskite capping layer incorporating the majority of the perovskite material is required. Recent reports have also shown equal or better performance in planar devices, while noting that one of the barriers to further performance enhancement is the film morphology, specifically film coverage and conformity to the underlying substrate.[11,12] Morphological holes in the active layer, due to incomplete coverage, reduce the generation of photocurrent and, more importantly, create shunt paths for photoexcited carriers. In 2013 alone there were multiple studies that investigated film processing parameters to improve the total film coverage by changing the annealing conditions,[13] coevaporation of both salts,[11] spin-coating the metal halide salt followed by soaking in the organic halide salt,[14] and spin-coating the metal halide salt followed by vapor deposition of the organic halide.[15] In spite of the positive impact these studies have had on film uniformity, there is still a lack of a fundamental understanding of the mechanisms leading to the final film and crystal morphology.

In studies of film evolution in both mesoporous and planar electrode configurations, we previously reported three distinct structure transitions including solution-to-precursor, precursor-to-perovskite, and perovskite-to-PbI_2.[5,16] The observation of a crystalline structure prior to the perovskite formation, as well as

Received: November 26, 2014
Published: January 27, 2015

DOI: 10.1021/ja512117e
J. Am. Chem. Soc. 2015, 137, 2350−2358

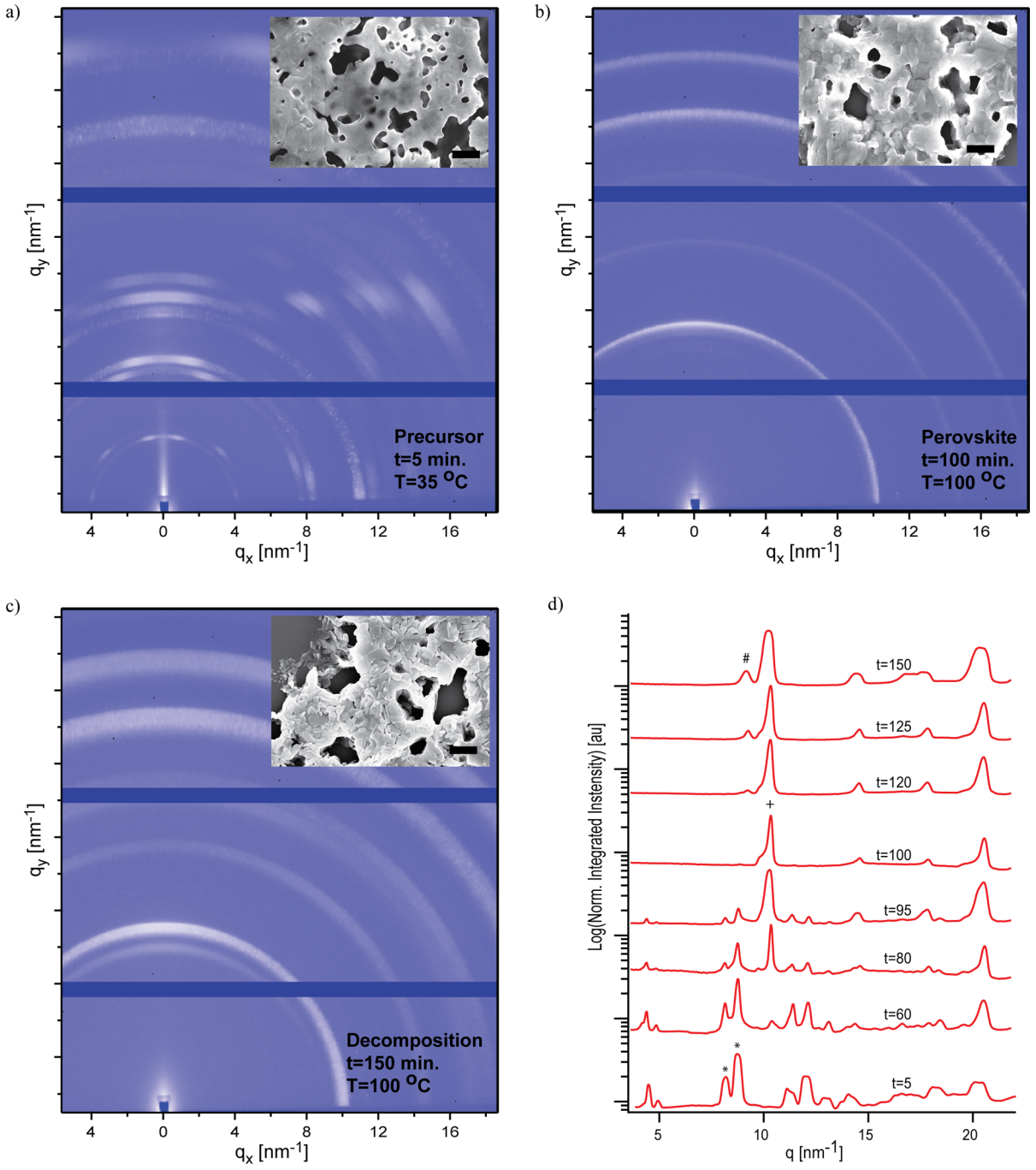

Figure 1. WAXS images (a–c) for 40 wt % solution of $PbCl_2$:(MA)I in a 1:3 molar ratio on Si, thermally annealed from ambient temperature to 100 °C: (a) precursor at t = 5 min and T = 35 °C, (b) perovskite at t = 100 min and T = 100 °C, and (c) PbI_2 (decomposition) at t = 150 min and T = 100 °C. Insets in parts a–c are corresponding SEM images with a 1 μm scale bar. (d) Corresponding azimuthally integrated 1D plots at key time points showing the overall structural evolution. Markers above traces at 5, 100, and 150 min indicate characteristic peak locations for the precursor (*), perovskite (+), and PbI_2 (#), respectively, that are used to track the transformations.[20,21]

the perovskite decomposition to lead iodide, has also been noted by others.[10,17] More recent studies have shown that the precursor material is a mixture of two (or more) materials and that at least one of these materials are lead halide clusters that may begin to form in solution.[18,19] These observations indicate that understanding the nature of the precursor material, and those factors that cause its transition to the perovskite, are keys to being able to predictably control the crystal and film growth.

Here, we turn our attention to the underlying kinetics of the precursor-to-perovskite transition. We begin by developing an appropriate methodology to analyze in situ, wide-angle X-ray scattering (WAXS) data to quantify the degree of perovskite formation when crystallizing in thin films. We verify our method by applying it to time/temperature structural evolution data and compare this analysis to a general model to validate its applicability. We use our validated method to analyze the crystallization dynamics of the perovskite when using different lead salts, in nonstoichiometric solutions, to extract the activation energy (E_a) for the transition. Finally, we use the E_a and WAXS patterns for the different systems we tested to

DOI: 10.1021/ja512117e
J. Am. Chem. Soc. 2015, 137, 2350–2358

determine the composition of the precursor and the role of the spectator species in the crystallization dynamics.

RESULTS AND DISCUSSION

Quantifying the Precursor-to-Perovskite Transformation. A kinetics study requires tracking the extent to which a transformation occurs in time; doing so requires both a qualitative and quantitative measure of both the starting and ending points of the transformation. In previous publications we have established these transitions qualitatively and refer the reader to refs 5 and 16 for complete details. Briefly, there are three distinct solid state structures that occur (in order, temporally): (1) a metastable, crystalline intermediate which we refer to as the precursor, (2) the desired perovskite, and (3) PbI_2, the decomposition product. In situ WAXS patterns, using conditions equivalent to those used to make working devices, were recorded and analyzed to establish the overall crystal evolution. Figure 1 shows representative 2D WAXS images for these three structures from thin films made from a non-stoichiometric solution of $PbCl_2$ and $(CH_3NH_3)I$, referred to as (MA)I, in a 1:3 molar ratio, as well as a waterfall plot that demonstrates the overall structural evolution.

In the course of our previous work, and in this study, several different processing parameters were explored including different deposition methods, varying temperature profiles, and changes to the lead salt reagent; in all cases the overall evolution is the same: precursor → perovskite → PbI_2. Regardless of the reagent salt used, we find the scattering pattern of the perovskite in excellent agreement with the tetragonal iodide perovskite; the agreement with the known peak locations of the iodide perovskite, along with elemental analysis recently published, confirms that we are making the iodide perovskite in all cases.[22] Furthermore, we established key scattering peaks associated with the precursor that are unique to its structure; given that the perovskite and PbI_2 structures are known, identification of scattering peaks unique to the precursor allows us to distinguish each of the structures qualitatively and quantitatively. For the perovskite and PbI_2 the key peaks are located at $q = 10$ nm^{-1} and $q = 9$ nm^{-1}, respectively, where q denotes the magnitude of the scattering vector and is defined as $q = 4\pi \sin\theta/\lambda$, where θ is half of the total scattering angle and λ is the X-ray wavelength. These peaks are chosen because they are strong, easily distinguishable, and in the low q range where they are not obscured by higher order reflections. The key peaks for the precursor structure change depending on the lead salt used, as is discussed in detail below. In all cases, however, there are key peaks below $q = 9$ nm^{-1}; since the smallest q vector for either the perovskite or PbI_2 is at $q = 9$ nm^{-1}, any peak below this value allows us to distinguish the precursor. These previous results provide the qualitative measure we need to identify each structure uniquely. In this study we are concerned with the precursor-to-perovskite transition, and the kinetic analysis requires an appropriate quantitative measure of the extent of the transformation.

The kinetic analysis of solid state transformations is commonly accomplished by determining the transformed fraction of a material, x, by tracking some property (e.g., conductivity, magnetism, modulus) that has different and known values for both the starting and ending states of the transformation.[21] In the present experiments, the WAXS data contain a direct measure of the quantity of diffracting planes with a specific orientation; this quantity is a measurable property that can be used to determine $x(t)$. The bottommost trace in Figure 1d shows that the strong reflection of (110) planes of the tetragonal perovskite structure at $q = 10$ nm^{-1} is not present in the precursor; hence, we track the (110) peak to determine x. Defining the integrated scattering intensity of the (110) peak as A_{10}, and given that this peak does not exist in the precursor, we can set $A_{10}(t = 0) = 0$; this is the known value for the starting state. To define a known value for A_{10} for the pure perovskite we note from Figure 1d (trace at $t = 100$ min) that there are no peaks below $q = 9$ nm^{-1} for the perovskite structure. We define a time, t_{end}, as the point in time when the peaks below $q = 9$ nm^{-1} completely disappear and use the measured value, $A_{10}(t_{end})$, to denote the property's value for the ending state. Mathematically, this gives the following definition for $x(t)$

$$x(t) \equiv \frac{A_{10}(t)}{A_{10}(t_{end})} \tag{1}$$

so that $x(0) = 0$ and $x(t_{end}) = 1$. The validity of the definition of $x(t)$ used here is based on a few assumptions.

The disappearance of the precursor peaks is due to the transformation to a different material (the perovskite) and not due to reorientation of the precursor grains such that the tracked peaks are no longer incident with the Ewald sphere. This assumption is justified as no new peaks appear during the transformation.

The transformation is a direct transition from the solid state precursor to the perovskite, as opposed to dissolution and recrystallization. In the case of dissolution there would be an increased volume of amorphous material, leading to an increase in the background scattering. We see no evidence of increased background scattering during the transformation (Supporting Information Figure S1) and take the assumption of a solid state transformation to be valid. It should be noted that there is some possibility that dissolution and recrystallization occurs at a temporal resolution finer than that used in the current experiments; although we cannot discount this possibility, it would not change the analysis or conclusions reached here.

There is no appreciable change in the crystallographic orientation of the perovskite crystals during the transformation. If the perovskite grains rotate during the transformation the resulting plots of $x(t)$ would not be monotonic; the data presented below shows monotonic, sigmoidal plots as expected for a solid state transformation. The quality of the fits to the mathematical model (discussed below), particularly in the linear portion of the plots, indicates that this assumption is also reasonable. We point out that a fixed orientation is only required for the perovskite and only during the transformation. The fact that the precursor and perovskite structures have different crystallographic orientations relative to each other, as well as different textures (Figure 1a,c), does not matter so long as they do not change relative to themselves. Additionally, after the initial point when $x(t) = 1$, i.e., the precursor is completely transformed, the perovskite can coarsen, and it does not affect the results as we are only concerned with the transition itself.

The initial system studied was the mixed halide system using $PbCl_2$ and (MA)I, which we will refer to as the chloride system, with full composition, deposition, and annealing details given in the Experimental Section. Given the above assumptions, we apply eq 1 to in situ WAXS data taken at ~3 min intervals until ~10−15 min after the precursor completely transforms; for the chloride system the precursor pattern shows clear peaks centered at $q \sim 7.9$ and 8.5 nm^{-1} (Figure 2a), and we use

DOI: 10.1021/ja512117e
J. Am. Chem. Soc. 2015, 137, 2350−2358

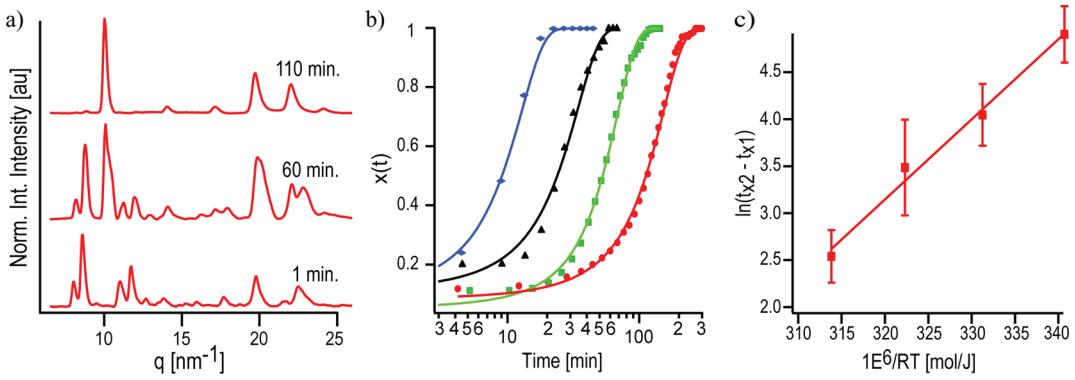

Figure 2. Kinetic data for isothermally annealed samples made from 40 wt % in DMF using $PbCl_2$ as the lead salt. (a) Azimuthally integrated WAXS data for the 90 °C sample showing the precursor (1 min), transition (60 min) and perovskite (110 min) stages of the transformation. (b) $x(t)$ plots for isothermal samples at 80 °C (red, circles), 90 °C (green, square), 100 °C (black, triangle), and 110 °C (blue, diamond) with the JMA model fits (eq 5, solid line of the same color); $x(t)$ is defined in the text. (c) Plot constructed from eq 2 to extract E_a, slope of the line is 86 ± 6 kJ/mol.

both in our analysis. This process yields the required time-dependent data to construct an $x(t)$ plot (Figure 2b), which is the quantitative measure of the transformation needed for a kinetics study.

Kinetic Modeling of the Precursor-to-Perovskite Transformation. Once a valid measure for $x(t)$ has been determined, kinetic parameters can be extracted by applying an appropriate model for the transformation. Mittemeijer and co-workers have done extensive work on the mathematical analysis of kinetic data for solid-state transformations for a wide variety of both nucleation and growth modes.[24−26] In addition to providing specific models for different systems, they also derive formulas for either isothermal or isochronal data that make no assumptions about the type of nucleation or growth; we use their formula for isothermal data here and refer the reader to ref 23 for detailed derivations:

$$\ln(t_{x2} - t_{x1}) = \frac{E_a}{RT} - \ln k_0 + \ln(\beta_{x2} - \beta_{x1}) \quad (2)$$

Here t_{xn} is the time at which the transformed fraction is x_n, E_a is the effective activation energy, R is the gas constant, T is the temperature, k_0 is the rate constant prefactor, and β_{xn} is a state property that is invariant to the time/temperature path. The introduction of β_{xn} assumes that there is some state property that is monotonically related to the physical property being measured; ergo, it is also related to the transformed fraction of the film, i.e., $x = F(\beta)$ where the form of F need not be known. To apply eq 2, data is plotted as $\ln(t_{x2} - t_{x1})$ versus $1/RT$ and the slope of the line taken as E_a; it should be noted that the extracted E_a is an effective activation energy for the transformation as a whole, where the activation energies for nucleation and growth are still coupled. Although the present data is insufficient to determine specific nucleation and growth modes, an effective E_a can still provide key insight into the crystallization process and the extent to which it can be affected by changes to the reaction chemistry.

Several films were prepared using the chloride system while changing only the annealing temperature. Isothermal data was taken at 80, 90, 100, and 110 °C and $x(t)$ extracted from the resulting WAXS data; the temperature range was chosen on the basis of previous reports that substantial crystallization does not occur below 80 °C and that a morphological change takes place at 130 °C.[6,17] Figure 2a shows representative 1D plots, at several key time points, taken from the 90 °C sample, with $x(t)$ for all four isothermal samples plotted in Figure 2b. As noted in the Experimental Section, data was taken at several locations on each film, and the resulting plots of $x(t)$ are the average of all sampled regions; as expected, the plots are sigmoidal, the rate of the transformation (the time axis in Figure 2b is log scale for clarity) increases with higher temperatures, and the transformation for the 100 °C sample (most commonly reported condition) is ∼60 min, in good agreement with the optimal annealing times found in device[22] and UV−vis absorption[18] studies. Starting and ending fractions of $x_1 = 0.2$ and $x_2 = 0.9$ were chosen and the corresponding times used in eq 2 to construct the plot in Figure 2c, which yields an effective activation energy of 86 ± 6 kJ/mol.

The nature of the $x(t)$ plots, their change with increasing temperature, and the quality of the linear fit in Figure 2c confirms that the methodology used is appropriate. We can further extend our kinetic analysis, then, by using the extracted E_a in an appropriate kinetic model. The Johnson−Mehl−Avrami (JMA) model has been widely used to describe solid state transformations and we apply it here in the well-known form[27]

$$x(t) = 1 - \exp(-\beta^n) \quad (3)$$

where n is the growth exponent, which describes the dimensionality of the growth and should be between 1 and 4. Due to the Arrhenius behavior of the system, we assume a simple rate equation for β in the form of:

$$\beta = k(T)t = k_0 \exp\left(\frac{-E_a}{RT}\right)t \quad (4)$$

where the variables used are the same as in eq 2, and plugging eq 4 into eq 3 gives the following:

$$x(t) = 1 - \exp\left[-\left(k_0 \exp\left(\frac{-E_a}{RT}\right)t\right)^n\right] \quad (5)$$

Equation 5 assumes that β follows Arrhenius behavior, E_a is not time dependent, and n is neither time nor temperature dependent. Fitting this model against our data, with E_a fixed at 86 kJ/mol, should yield constant values for k_0 and n. The best fits of eq 5 describe the data well, as shown in Figure 2b, with $k_0 = 4.1 \times 10^{10} \pm 9.3 \times 10^9$ and $n = 2.43 \pm 0.06$; it should be noted that the fits were performed with those data points where $x(t) \geq 0.2$ heavily weighted as the signal-to-noise ratio increases dramatically at higher values of x. The extracted values are not only effectively constant for all temperatures, but the value of

DOI: 10.1021/ja512117e
J. Am. Chem. Soc. 2015, 137, 2350−2358

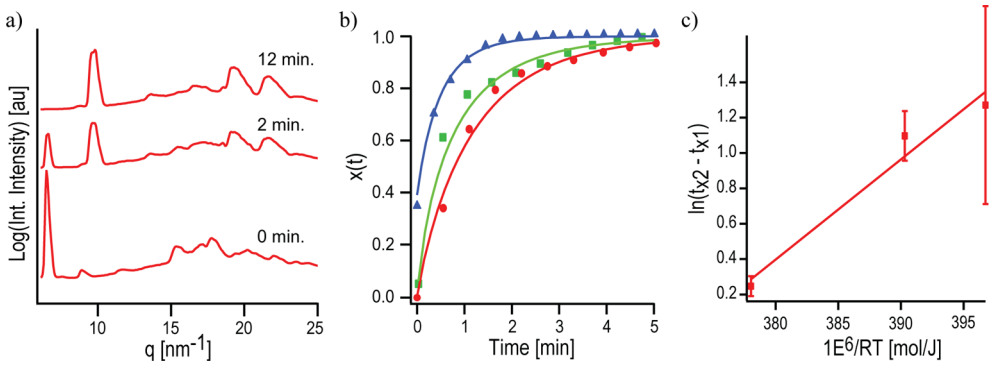

Figure 3. Kinetic data for isothermally annealed samples made from 40 wt % in DMF using $Pb(NO_3)_2$ as the lead salt. (a) Azimuthally integrated WAXS data for the 30 °C sample showing the precursor (0 min), transition (2 min), and perovskite (12 min) stages of the transformation. (b) $x(t)$ plots for isothermal samples at 30 °C (red, circles), 35 °C (green, square), and 45 °C (blue, triangle) with the JMA model fits (eq 5, solid line of the same color); $x(t)$ is defined in the text. (c) Plot constructed from eq 2 to extract E_a; the slope of the line was found to be 56.6 ± 10 kJ/mol.

the growth exponent is reasonable for 2D thin films in the context of the JMA model. We point out that these fits were done in two steps, with E_a calculated using eq 2 and the resulting value used in eq 5; as such, we have not decoupled the nucleation and growth modes. Therefore, in spite of the agreement between the model and the data, we take the JMA model to be a good mathematical description of the system, but only phenomenologically; the values of k_0 and n should be taken as empirical fit parameters.

Application of the Model. In order to apply a purely mathematical description at least one additional system needs to be analyzed; this would establish that a change in the crystallization time is due to a change in E_a versus a change in k_0 and/or n. Experimentally, it would be most efficient to have a methodology by which processing conditions (e.g., changing the lead salt reagent) could be altered at a single, random temperature, and a qualitative assessment made as to the impact on the crystallization kinetics. Since eq 5 represents only a mathematical description of the film evolution, and because the current data set provides no information about specific nucleation and growth modes, k_0 and n remain coupled. Therefore, we repeated a complete isothermal analysis on a second system to verify that n remains constant when changing the lead salt reagent, allowing us to apply eq 5 to any additional system at a single temperature.

In a previous report we examined perovskite films crystallized from a nonhalide lead source, $Pb(NO_3)_2$,[28] and found that the crystallization occurred much faster and at lower temperatures than either the iodide or chloride system. We chose the nitrate system, as a second system to analyze, due to the fact that the resulting data points would be widely disparate in both their temperature and time. Samples were prepared using identical conditions to those of the chloride samples shown in Figure 2 with only the following changes: (1) the solution was 1:3 molar ratio of $Pb(NO_3)_2$:(MA)I, and (2) the temperatures used were 30, 35, and 45 °C. The data set was collected and analyzed using the same methodology and yielded the plots in Figure 3 [the time axis in Figure 3b is linear versus log (t) in Figure 2b]. Due to the speed with which the nitrate based films formed and the constraints of the chosen experimental setup, capturing the entire transformation was difficult, particularly at higher temperatures. In spite of a lower signal-to-noise ratio (temporally), Figure 3 shows that the nitrate system is similarly well-described by the analysis method used.

For the nitrate system our analysis yields $E_a = 56.6 \pm 10$ kJ/mol, with $k_0 = 2.0 \times 10^9 \pm 8.1 \times 10^8$ and $n = 2.34 \pm 0.09$; these values change as expected confirming that the JMA model is appropriate and inferring that the overall crystallization process is not changed by a change to the lead salt. To the extent that the time/temperature required for complete transformation of the nitrate system is a kinetic effect, and not the result of a fundamentally different crystallization mechanism, we expect E_a and k_0 to be different while n should be the same. In terms of applying the methodology to changing the lead salt, the results indicate that the difference between the chloride and nitrate systems lies in the effective E_a. This approach allows for a qualitative comparison of different systems whose processing cannot be accomplished at the same temperatures used for the complete isothermal data sets.

Mathematically, the determination of the kinetic parameters required a two-step approach: eq 2 to extract E_a, followed by eq 5 for k_0 and n. This was due to the coupling of parameters noted above. The application of the model to a second, complete, isothermal data set confirms that n is a constant. On the basis of the assumption that a change in the lead salt does not change the overall crystallization process, we can now fit eq 5 by fixing n and using k_0 and E_a as the two free parameters which allows the extraction of E_a for additional systems at a single temperature as it only requires a single $x(t)$ plot.

Dependency of Activation Energy on the Lead Salt. We complete our kinetics study by looking at the evolution of two additional systems, made using lead acetate and lead iodide, at a single temperature. We chose to explore changes to the lead salt because its role in nonstoichiometric systems remains open and relevant to increased device performance on the basis of the enhanced transport properties and charge carrier lifetimes of films made using the chloride system.[29] In those cases where some or all of the lead salt anion is not incorporated into the perovskite, there is a spectator salt, (MA)Sp, remaining due to the nonstoichiometric salt ratios used:

$$PbSp_2 + 3(MA)I \rightarrow (MA)PbI_3 + 2(MA)Sp \quad (6)$$

Therefore, exploring different lead sources is synonymous with exploring the role of the spectator salt. The acetate system was developed by Zhang et al.[22] The complete data set can be found in ref 22, and we only present the extracted kinetic data for that system in this paper. The iodide films were prepared from a nonstoichiometric solution, using a 3:1 molar ratio of

DOI: 10.1021/ja512117e
J. Am. Chem. Soc. 2015, 137, 2350−2358

(MA)I:PbI_2 and annealed at 150 °C. The annealing temperatures used for the iodide and acetate systems correspond to the temperatures yielding the best device performance, also reported in ref 22.

The Δt between x = 0.2 and x = 0.9 for the acetate system, annealed at 100 °C, was found to be 1.14 min (the same Δt for the chloride system at 100 °C is 12.7 min); by direct comparison, the kinetics of the acetate are faster than those for the chloride system, and by extrapolation of the nitrate to 100 °C, slower than those of the nitrate system. Fitting eq 5 to the single $x(t)$ plot, black diamonds in Figure 4a, with n constrained to 2.4 ± 0.1, results in the solid black fit line in Figure 4a and a value of E_a = 67.5 kJ/mol. As expected, this value for E_a is between that of the chloride and nitrate systems. The Δt between x = 0.2 and x = 0.9 for the iodide system, annealed at 150 °C, was found to be 11.6 min; given that Δt for the same transformed fraction of the chloride system at 110 °C is 12.7 min, it is obvious that the iodide system is slower. We repeat the same analysis as for the acetate system, and the resulting plot of $x(t)$ with the fit to eq 5 is shown in Figure 4a (red, circles). Figure 4b shows the Arrhenius plots for both the chloride and nitrate systems with their best fits as solid lines. For the acetate and iodide systems the single data points have been added and lines (dashed) constructed for each using the slope determined by eq 5. The complete results, for all four systems, are tabulated in Table 1; it is important to note that the values extracted here are limited to the specific processing conditions used. For example, processing thin films of (MA)PbI_3 in humid air is known to accelerate the crystallization and decomposition;[16] the activation energy is likely higher for films made entirely in an inert environment. We also note that recent reports have shown evidence that nucleation of the perovskite is seeded by lead halide clusters, which may begin forming in the solution phase,[19] and that the precursor material is a mixture of at least two materials[18] (presumably one of which is the lead halide clusters). The implication of these new findings can be seen in the nitrate and acetate data where we do not capture the pure precursor and, therefore, cannot tell whether growth begins in the solution phase or is simply too fast for the current experimental setup. In either case, this highlights the fact that the current methodology leaves the nucleation and growth modes coupled, and the values for k_0 and n should be taken as empirical values.

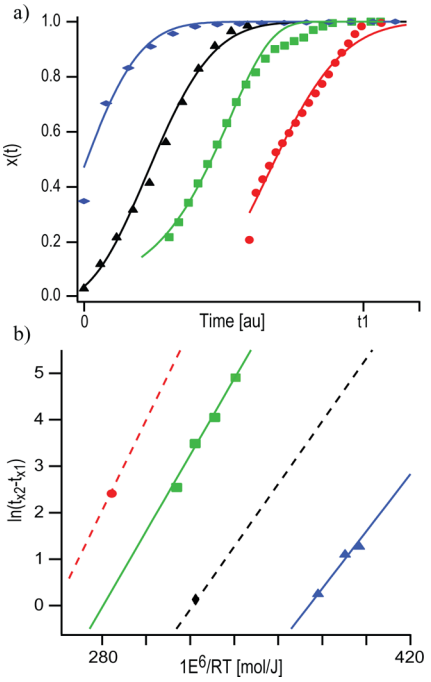

Figure 4. Kinetic data for all four systems prepared from a 40 wt % solution in DMF using different lead salts: (a) $x(t)$ plots for the nitrate (blue, diamond), acetate (black, triangle), chloride (green, square), and iodide (red, circle) systems annealed at 45, 100, 100, and 150 °C, respectively; data is scaled on the abscissa so that t_{end} (defined in text) is coincident for all traces, and then offset for clarity. Solid lines are the best fit lines of a global fit to eq 5. (b) Arrhenius plots for the same four systems (same colors/shapes as above) with best fit lines (solid) and calculated fit lines (dashed) using E_a extracted from part a.

Table 1. Extracted Parameters from Equation 5 for All Four Systems Based on the Global Fit Shown in Figure 4a

system	temp (°C)	E_a (kJ/mol)	k_0 (au)	n
iodide	150	97.3	6.8×10^{10}	2.4
chloride	90	86.6	4.1×10^{10}	2.4
acetate	100	67.5	2.1×10^{9}	2.4
nitrate	45	56.6	2.3×10^{9}	2.4

Ex situ absorption data on completely annealed films (Supporting Information Figure S3) show a band gap of ~1.6 eV, the known bandgap of the tri-iodide perovskite. This absorption data, along with the accompanying WAXS patterns, and elemental analysis reported by others, confirm that chloride is not substantially incorporated into the iodide structure.[18,30,31] Given that (MA)PbI_3 is the structure we are forming in all cases, the change in E_a for the different systems is only a function of the change in the lead salt used. The fact that changing the lead salt effects E_a for the crystallization provides key insight into the nature of the precursor structure as well as the overall crystallization process.

Precursor Phase and the Role of the Spectator Salt. As previously stated, understanding the nature of the precursor is an important step to controlling the final film morphology. In this section, we use the scattering patterns along with the kinetic data derived above to determine the composition for the precursor and the process by which the transformation to the perovskite occurs. Full understanding of the precursor would also include stoichiometric and structural information, both of which are experimentally difficult due to the metastability of the precursor and its compositional ambiguity; i.e., the precursor cannot be readily purified and we do not know what it is. Other researchers have attempted this and reported partial results, but the issues noted here continue to make elemental analysis (stoichiometry) and crystallography (structure) of the precursor difficult.[10,32−34] We note that ref 10, from Seok et al., postulates that the precursor structure is due to incorporated solvent. In their study the films were made with stoichiometric ratios of PbI_2 and (MA)I, and so, there is no spectator salt in the way that we have defined it here. Because the systems studied were different, and because we do not have sufficient detail on their characterization methods, we cannot comment on the difference in our results other than to say we see no evidence of solvent incorporation in our scattering data (Figure 5).

The kinetics analysis performed in this study was facilitated by the fact that each system has a precursor scattering pattern distinguishable from the final perovskite structure. The 2D WAXS patterns (Supporting Information Figure S2) of the

DOI: 10.1021/ja512117e
J. Am. Chem. Soc. 2015, 137, 2350−2358

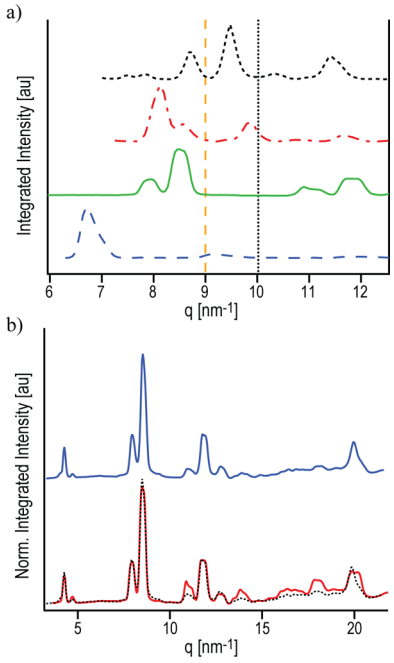

Figure 5. 1D, normalized, integrated WAXS data for thin films within 3 min of spin coating (a) using the same solvent but a different lead salt including acetate (black, dot), iodide (red, dot-dash), chloride (green, solid), and nitrate (blue, dash); vertical markers are the lowest q-vector reflection positions for PbI_2 (yellow, dash) and $(MA)PbI_3$ (black, dot). (b) With the same lead salt (chloride) but different solvents, DMF (red, solid) and DMSO (blue, solid), the DMSO trace is shown a second time as a black dotted line superimposed on top of the DMF trace facilitating direct comparison.

precursor structures clearly show that the precursor is a crystalline structure with a high degree of orientation in the film normal direction. Figure 5a shows the 1D patterns, in the low q range where the distinctive precursor peaks appear, for all four systems prepared using identical processing with the exception of the lead salt. The fact that the precursor scattering pattern is different for each lead salt used is clear evidence that the precursor structure contains the spectator salt. The only other component in the film is the solvent, and to check for incorporation of the solvent we prepared films using the chloride system with identical processing while changing only the solvent. Figure 5b shows the resulting 1D scattering patterns; the excellent agreement in the scattering patterns of films made from DMF and DMSO demonstrates that the resulting structure has no dependence on the solvent used. We therefore discern that there is no incorporated solvent in the precursor structure. These results suggest that the precursor structure is composed of Pb^{2+}, $(MA)^+$, I^-, and Sp^- ions where Sp^- denotes the anion of the spectator salt. Although assignment of a structure or stoichiometry to the precursor was not the subject of this study, this analysis provides clear determination of the composition. This in turn provides insights into the kinetic data derived above as well as the overall process by which the perovskite forms.

The composition of the precursor, taken with the activation energy for each system, demonstrates that the precursor-to-perovskite transition includes, and is dominated by, the removal of the excess spectator salt from the precursor. At this point we can make no assignment of cause and effect, i.e., if the migration of the spectator ions causes the perovskite transition or if the perovskite transition causes the migration of the spectator ions. Additionally, any mechanistic insight is beyond the scope of this work although certainly determination of the cause and effect, as well as the mechanism by which it occurs, is a logical next step to a better fundamental understanding of these systems. In spite of these unanswered questions, the current insight is valuable in that it tells us that the crystallization process can be mediated by changes to the lead salt.

As a final step in our analysis, we use the extracted E_a, along with a variety of published and internal data, to propose a crystallization path and explain some of the results of this and previous studies. Figure 6 is a schematic representation of the

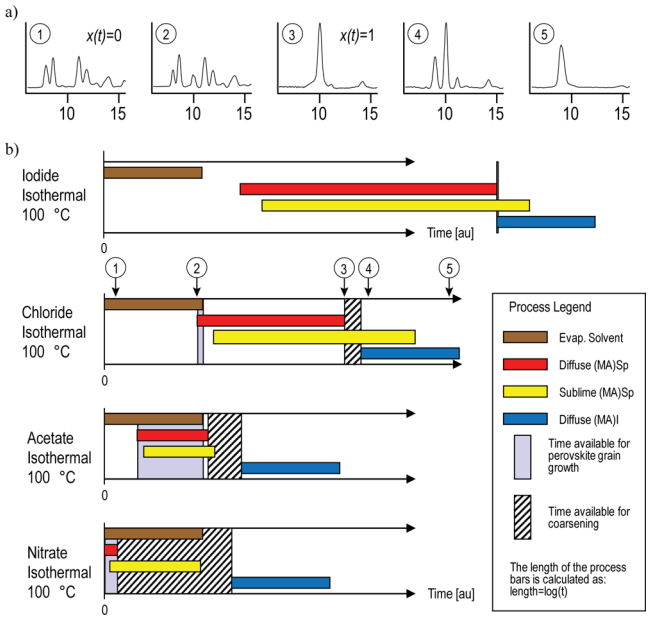

Figure 6. Schematic representation of the perovskite crystallization and growth pathway as a function of lead anion. (a) Scattering data for key time points for the chloride system (same sample as Figure 1) with the normalized, integrated intensity plotted against q [nm^{-1}]; the correlation of each scattering image in part a to the schematic timeline is shown in part b for the chloride system. (b) Schematic timelines for the four lead salt systems used in this study. The legend shows the title for each colored bar with the full explanation of the process given in the text. Although the pathway timeline is intended to be schematic, the start time and length for each process are calculated from data (see Supporting Information for details) to be as accurate as our data allows.

crystallization pathway along with the corresponding scattering plots for key points in the crystal evolution. The Supporting Information contains a complete description of how the start time and length were determined for each process bar shown; although we have taken great care to be as accurate as possible, the diagram shown is intended to be schematic in nature. The important point of this diagram is to identify the key processes, both advantageous and disadvantageous, and show how they are coupled in time. Knowledge of the precursor composition allows us to identify these processes as evaporation of the solvent ("Evap. Solvent", brown), diffusion of the excess spectator salt out of the precursor structure ("Diffuse (MA)Sp", red), removal of the spectator salt from the film ("Sublime (MA)Sp", yellow), and removal of stoichiometric (MA)I from the perovskite lattice ("Diffuse (MA)I", blue). The diffusion of

DOI: 10.1021/ja512117e
J. Am. Chem. Soc. 2015, 137, 2350−2358

the spectator salt from the precursor is, effectively, the transition measured in this study, with its start and end points coinciding with the start and end of the precursor−perovskite transition. The diffusion of (MA)I from the perovskite lattice is a disadvantageous process that corresponds to the decomposition to PbI_2.

For the iodide system, the high E_a, and the low volatility of the spectator salt, requires processing times and temperatures longer than those needed to evaporate the solvent but similar to those needed for decomposition. As a result, grain growth time is negligible, and coarsening time is limited by the decomposition process. This elucidates one key role of the chloride, which is to advantageously affect the crystallization kinetics. When lead chloride is used, the crystallization process can proceed at lower temperatures; Graetzel and co-workers, and our previous reports, fix the onset of crystallization at ∼75−80 °C, versus ∼100−110 °C for the iodide.[16,17] TGA data from our lab (Supporting Information, Figure S4), taken on thin film samples prepared under equivalent conditions to those used in the X-ray studies, show that there is still some solvent remaining at the onset of the transition when using the chloride system as reflected in Figure 6. As a result, there is some time available for grain growth. Additionally, the lower E_a for the chloride system expands the coarsening window by extending the time between the end of the transition and the onset of decomposition. The acetate system has a low enough E_a that the crystallization occurs much faster and is complete with appreciable solvent still in the film and well before the onset of decomposition. Even though the annealing temperature used is the same as the chloride, the crystal growth is decoupled from both the salt removal and decomposition in time. In the previously referenced acetate report,[22] we provide evidence that the acetate is the only system we studied that shows coarsening of the crystal domains after complete crystallization, and we refer the reader to that paper for details on the advantageous impact on both film morphology and the resulting device performance. Finally, in the nitrate system the three processes are decoupled in both time and temperature; the crystallization can occur in minutes and at room temperature. In fact, these three processes are so well-decoupled that the salt removal can be accomplished by rinsing with a good antisolvent for the perovskite rather than by heat. Unfortunately, the nitrate system has such a low E_a that the driving force for crystal growth, even at room temperature, is high enough to cause spherulitic growth which results in poor film morphology.[28]

Although Figure 6 is only intended to be a schematic representation of the crystallization processes, it elucidates several key aspects of the film and crystal growth. First, the most widely reported systems, iodide and chloride, have very narrow processing windows, and there is a high likelihood that films made at different times or in different laboratories would have a large deviation in their crystal properties and the film composition (e.g., the amount of remaining spectator salt). Second, Figure 6 highlights the importance of decoupling the desired and undesired processes from each other and the impact that has on broadening the windows for grain growth and coarsening. Decoupling these two processes cannot be accomplished by temperature alone, and a second parameter is needed to fully tune the growth; one principal result of this study is the use of the activation energy as a second parameter. The kinetic effects of the lead salt provide a manner in which the desired processes can be decoupled from the undesired processes independent of the temperature.

CONCLUSION

We developed a method to extract the transformed fraction, $x(t)$, of methylammonium lead trihalide perovskite films by analysis of in situ WAXS data and used this fraction to select an appropriate kinetics model. We applied this model to extract the activation energy for the precursor-to-perovskite transition in thin films when depositing nonstoichiometric ratios of lead and methylammonium salts in DMF and showed that the change in E_a is strongly dependent on the lead salt used. Finally, we added this knowledge of E_a to previously reported data to discern the compositional elements for the precursor and showed that controlling E_a, by changing the lead salt, allows for better crystal growth and has measurable and advantageous effects on the film morphology.

EXPERIMENTAL SECTION

Materials. All materials were used as received. Chloroform (anhydrous), *N*,*N*-dimethylformamide (DMF, anhydrous), ethanol (absolute), titanium(IV) isopropoxide (>97%), hydriodic acid (57 wt % in water), methylamine (33 wt % in ethanol), lead(II) nitrate ($Pb(NO_3)_2$), lead(II) acetate ($PbAc_2$), lead(II) iodide (PbI_2), and lead(II) chloride ($PbCl_2$) were obtained from Sigma-Aldrich (St. Louis, MO).

Salt and Solution Preparation. Methylammonium iodide, (MA)I, was prepared as previously published and stored in a desiccator.[9] Both organic and inorganic salts were pumped down in the glovebox antechamber overnight to remove any residual water. A 40 wt % solution of PbX_2 (where X = Cl, I, Ac, or NO_3) and (MA)I in a 1:3 molar ratio was prepared in a nitrogen glovebox by dissolving in DMF and stirring at low speed overnight. An appropriate volume of the mother solution was removed in a sealed container and only exposed to ambient air at the time of film preparation.

Substrate Preparation. Films were made on silicon or glass substrates that had been cleaned by sequential sonication in acetone and then isopropyl alcohol (IPA) for 5 min followed by rinsing with IPA and deionized (DI) water and then UV-ozone (UVO) cleaning for 5 min. Just prior to spin coating the substrates were rinsed with IPA and DI water, dried under nitrogen flow, and cleaned with UVO for 1−2 min.

Film Preparation. Perovskite films were made by depositing ∼60 μL of 40 wt % solution and spinning at 2500 rpm for 30 s. Upon removal from the spin-coater the substrates were placed on a heating stage in air that had been preheated to the annealing temperature noted in the text. The transfer time from the spin-coater to the heating stage was typically 2−3 min; the time between placing the substrate on the preheated stage and the first image was typically 30−90 s. Thermal treatment for films used in Figure 1 included a ramp from room temperature to the annealing temperature as detailed in reference 16.

WAXS Characterization. Samples were spin-coated at the Cornell High Energy Synchrotron Source (CHESS) and loaded on a custom-built temperature-controlled grazing incidence stage at the D1 beamline,[35] with a typical transfer period of 2−3 min. Two different detectors were used during the different runs: (a) Fuji image plates, 2500 × 2000 pixels with 100 μm/pixel resolution, placed in a holder at a distance of 177 mm and digitized using a GE Healthcare Typhoon FLA-7000 image plate reader, and (b) Pilatus 3 300 K high speed pixel array detector, 487 × 619 pixels with 172 μm/pixel resolution, at a distance of 107.5 mm from the sample. The X-ray wavelengths were set at 0.1161 and 0.1155 nm, respectively, for the different detectors. In both runs the incident beam angle was about 0.5°, well above the substrate critical angle. Typical exposure times were <2 s. To avoid beam induced damage in the perovskite films at higher beam flux, the sample was moved perpendicular to the beam in 0.5 mm increments (the nominal beam width), and data collected from 16 to 28 different

DOI: 10.1021/ja512117e
J. Am. Chem. Soc. 2015, 137, 2350−2358

locations on the same substrate depending on the exact dimensions of the substrate used.

2D WAXS images were integrated using the Fit2D software package from ESRF; background subtraction, the integrated peak area determinations, and the calculation of $x(t)$ were performed using IGOR, a commercially available software product.

Thermogravimetric Analysis (TGA). TGA was performed on a Seiko Instruments (SII) Exstar TG/DTA 6200 using dry nitrogen as a purge gas. Samples were prepared as noted in the "Film Preparation" section using $PbCl_2$ as the lead source, and substrates were 8 mm × 8 mm glass coverslips. Heating profile consisted of 60 min at 30 °C, followed by a ramp of 1 °C/min to 200 °C.

■ ASSOCIATED CONTENT

Supporting Information

Integrated WAXS patterns showing constant background signal, representative 2D WAXS images and the corresponding 1D integrations for all four lead salt systems, the methodology used to calculate the process bars for Figure 6, and TGA data. This material is available free of charge via the Internet at http://pubs.acs.org

■ AUTHOR INFORMATION

Corresponding Authors

ubw1@cornell.edu
lae37@cornell.edu

Present Address

[⊥]Simpson Querrey Institute for BioNanotechnology, Northwestern University, Evanston, Illinois, 60208, United States.

Notes

The authors declare no competing financial interest.

■ ACKNOWLEDGMENTS

The authors acknowledge financial support from the U.S. Department of Energy, Office of Science, Basic Energy Sciences, under Award DE-SC0010560. K.W.T. gratefully acknowledges the Singapore Energy Innovation Program Office for a National Research Foundation graduate fellowship. This work made use of the research facilities of the Cornell Center for Materials Research (CCMR) with support from the NSF Materials Research Science and Engineering Centers (MRSEC) program (DMR-1120296), Cornell High Energy Synchrotron Source (CHESS) which is supported by the NSF and the NIH/National Institute of General Medical Sciences under NSF awards DMR-0936384 and DMR-1332208, and the KAUST-Cornell Center for Energy and Sustainability supported by Award KUS-C1-018-02, made by King Abdullah University of Science and Technology (KAUST). W.Z. and H.J.S thank the EPSRC Supergen, ERC Hyper Project, for financial support. The authors acknowledge the use of Fit2D for WAXS data analysis and thank the author, A. P. Hammersley, and ESRF, for its development and free use. The authors gratefully acknowledge T. Scott, M. Koker, and R. Li of Cornell University for kind experimental assistance.

■ REFERENCES

(1) McGehee, M. D. *Nature* **2013**, *501*, 323.
(2) Snaith, H. J. *J. Phys. Chem. Lett.* **2013**, *4*, 3623.
(3) Kazim, S.; Nazeeruddin, M. K.; Grätzel, M.; Ahmad, S. *Angew. Chem., Int. Ed.* **2014**, *53*, 2812.
(4) Zhou, H.; Chen, Q.; Li, G.; Luo, S.; Song, T. -b.; Duan, H.-S.; Hong, Z.; You, J.; Liu, Y.; Yang, Y. *Science* **2014**, *345*, 542.
(5) Saliba, M.; Tan, K. W.; Sai, H.; Moore, D. T.; Scott, T.; Zhang, W.; Estroff, L. A.; Wiesner, U.; Snaith, H. J. *J. Phys. Chem. C* **2014**, *118*, 17171.
(6) Xiao, Z.; Dong, Q.; Bi, C.; Shao, Y.; Yuan, Y.; Huang, J. *Adv. Mater.* **2014**, *26*, 6503.
(7) Im, J.-H.; Jang, I.-H.; Pellet, N.; Grätzel, M.; Park, N.-G. *Nat. Nanotechnol.* **2014**, *9*, 923.
(8) Kim, H.-S.; Lee, C.-R.; Im, J.-H.; Lee, K.-B.; Moehl, T.; Marchioro, A.; Moon, S.-J.; Humphry-Baker, R.; Yum, J.-H.; Moser, J. E.; Grätzel, M.; Park, N.-G. *Sci. Rep.* **2012**, *2*, 591.
(9) Lee, M. M.; Teuscher, J.; Miyasaka, T.; Murakami, T. N.; Snaith, H. J. *Science* **2012**, *338*, 643.
(10) Jeon, N. J.; Noh, J. H.; Kim, Y. C.; Yang, W. S.; Ryu, S.; Seok, S. Il. *Nat. Mater.* **2014**, *13*, 897.
(11) Liu, M.; Johnston, M. B.; Snaith, H. J. *Nature* **2013**, *501*, 395.
(12) Conings, B.; Baeten, L.; De Dobbelaere, C.; D'Haen, J.; Manca, J.; Boyen, H.-G. *Adv. Mater.* **2014**, *26*, 2041.
(13) Eperon, G. E.; Burlakov, V. M.; Docampo, P.; Goriely, A.; Snaith, H. J. *Adv. Funct. Mater.* **2014**, *24*, 151.
(14) Liu, D.; Kelly, T. L. *Nat. Photonics* **2013**, *8*, 133.
(15) Chen, Q.; Zhou, H.; Hong, Z.; Luo, S.; Duan, H.-S.; Wang, H.-H.; Liu, Y.; Li, G.; Yang, Y. *J. Am. Chem. Soc.* **2014**, *136*, 622.
(16) Tan, K. W.; Moore, D. T.; Saliba, M.; Sai, H.; Estroff, L. A.; Hanrath, T.; Snaith, H. J.; Wiesner, U. *ACS Nano* **2014**, *8*, 4730.
(17) Dualeh, A.; Tétreault, N.; Moehl, T.; Gao, P.; Nazeeruddin, M. K.; Grätzel, M. *Adv. Funct. Mater.* **2014**, *24*, 3250.
(18) Unger, E. L.; Bowring, A. R.; Tassone, C. J.; Pool, V.; Gold-Parker, A.; Cheacharoen, R.; Stone, K. H.; Hoke, E. T.; Toney, M. F.; McGehee, M. D. *Chem. Mater.* **2014**, DOI: 10.1021/cm503828b.
(19) Tidhar, Y.; Edri, E.; Weissman, H.; Zohar, D.; Hodes, G.; Cahen, D.; Rybtchinski, B.; Kirmayer, S. *J. Am. Chem. Soc.* **2014**, *136*, 13249.
(20) Mitchell, R. S. *Z. Kristallogr.* **1959**, *111*, 372.
(21) Colella, S.; Mosconi, E.; Fedeli, P.; Listorti, A.; Gazza, F.; Orlandi, F.; Ferro, P.; Besagni, T.; Rizzo, A.; Calestani, G.; Gigli, G.; De Angelis, F.; Mosca, R. *Chem. Mater.* **2013**, *25*, 4613.
(22) Zhang, W.; Saliba, M.; Moore, D. T.; Pathak, S. K.; Hörantner, M. T.; Stergiopoulos, T.; Stranks, S.; Eperon, G. E.; Webber, J. A.; Abate, A.; Sadhanala, A.; Yao, S.; Chen, Y.; Friend, R. H.; Estroff, L. A.; Wiesner, U.; Snaith, H. J. *Nat. Commun.* **2014**, *6*, 6142.
(23) Hadjichristidis, N.; Pispas, S.; Floudas, G. In *Block Copolymers: Synthetic Strategies, Physical Properties, and Applications*; John Wiley & Sons, Inc.: Hoboken, NJ, 2003; pp 313−334.
(24) Mittemeijer, E. J. *J. Mater. Sci.* **1992**, *27*, 3977.
(25) Liu, F.; Sommer, F.; Mittemeijer, E. J. *J. Mater. Sci.* **2006**, *42*, 573.
(26) Liu, F.; Sommer, F.; Bos, C.; Mittemeijer, E. J. *Int. Mater. Rev.* **2007**, *52*, 193.
(27) Avrami, M. *J. Chem. Phys.* **1940**, *8*, 212.
(28) Moore, D. T.; Sai, H.; Wee Tan, K.; Estroff, L. a.; Wiesner, U. *APL Mater.* **2014**, *2*, 081802.
(29) Edri, E.; Kirmayer, S.; Henning, A.; Mukhopadhyay, S.; Gartsman, K.; Rosenwaks, Y.; Hodes, G.; Cahen, D. *Nano Lett.* **2014**, *14*, 1000.
(30) You, J.; Hong, Z.; Yang, Y. M.; Chen, Q.; Cai, M.; Song, T.; Chen, C.; Lu, S.; Liu, Y.; Zhou, H.; Yang, Y. *ACS Nano* **2014**, *8*, 1674.
(31) Zhao, Y.; Zhu, K. *J. Phys. Chem. C* **2014**, *118*, 9412.
(32) Yu, H.; Wang, F.; Xie, F.; Li, W.; Chen, J.; Zhao, N. *Adv. Funct. Mater.* **2014**, *45*, 7102.
(33) Williams, A. E.; Holliman, P. J.; Carnie, M. J.; Davies, M. L.; Worsley, D. A.; Watson, T. M. *J. Mater. Chem. A* **2014**, *2*, 19338.
(34) Williams, S. T.; Zuo, F.; Chueh, C.; Liao, C.; Liang, P.; Jen, A. K.-Y. *ACS Nano* **2014**, *8*, 10640.
(35) Bian, K.; Choi, J. J.; Kaushik, A.; Clancy, P.; Smilgies, D.; Hanrath, T. *ACS Nano* **2011**, *5*, 2815.

DOI: 10.1021/ja512117e
J. Am. Chem. Soc. 2015, 137, 2350−2358